electronics

MDPI

Article

Development and Evaluation of a Piezoelectret Insole for Energy Harvesting Applications

Marcio L. M. Amorim [1], Gabriel Augusto Ginja [1,†], Melkzedekue de Moraes Alcântara Calabrese Moreira [1,2,†], Oswaldo Hideo Ando Junior [3], Adriano Almeida Goncalves Siqueira [2], Vitor Monteiro [6], José A. Afonso [4,5], João P. P. do Carmo [1] and João L. Afonso [6,*]

[1] Group of Metamaterials Microwaves and Optics (GMeta), Department of Electrical Engineering (SEL), University of São Paulo (USP), Avenida Trabalhador São-Carlense, Nr. 400, Parque Industrial Arnold Schimidt, São Carlos 13566-590, SP, Brazil; marciolma@usp.br (M.L.M.A.); gabriel.ginja@sc.usp.br (G.A.G.)
[2] Department of Mechancial Engineering (SEM), University of São Paulo (USP), Avenida Trabalhador São-Carlense, Nr. 400, Parque Industrial Arnold Schimidt, São Carlos 13566-590, SP, Brazil; siqueira@sc.usp.br
[3] Research Group on Energy & Energy Sustainability (GPEnSE), Center for Alternative and Renewable Research (CEAR), Federal University of Paraiba (UFPB), João Pessoa 58051-900, PB, Brazil; oswaldo.junior@cear.ufpbr.br
[4] CMEMS-UMinho, University of Minho, Campus de Azurém, 4800-058 Guimarães, Portugal; jose.afonso@dei.uminho.pt
[5] LABBELS—Associate Laboratory, Campus de Gualtar, 4710-057 Braga, Portugal
[6] ALGORITMI Research Centre/LASI, University of Minho, 4800-058 Guimarães, Portugal
* Correspondence: jla@dei.uminho.pt
† These authors contributed equally to this work.

Abstract

This work presents the development and experimental validation of a low-cost, piezoelectret-based energy harvesting system integrated into a custom insole, as a promising alternative for future self-powered wearable electronics. The design utilizes eight thermoformed Teflon piezoelectrets, strategically positioned in high-impact regions (heel and forefoot), to convert footstep-induced mechanical motion into electrical energy. The sensors, fabricated using Fluorinated Ethylene Propylene (FEP) and Polytetrafluoroethylene (PTFE) layers via thermal pressing and aluminum sputtering, were connected in parallel to enhance signal consistency and robustness. A solenoid-actuated mechanical test rig was developed to simulate human gait under controlled conditions. The system consistently produced voltage pulses with peaks up to 13 V and durations exceeding ms, even under limited-force loading (10 kgf). Signal analysis confirmed repeatable waveform characteristics, and a Delon voltage multiplier enabled partial conversion into usable DC output. While not yet optimized for maximum efficiency, the proposed setup demonstrates the feasibility of using piezoelectrets for energy harvesting. Its simplicity, scalability, and low cost support its potential for future integration in applications such as fitness tracking, health monitoring, and GPS ultimately contributing to the development of autonomous, self-powered smart footwear systems. It is important to emphasize that the present study is a proof-of-concept validated exclusively under controlled laboratory conditions using a mechanical gait simulator. Future work will address real-time insole application tests with human participants.

Keywords: energy harvesting; human gait simulation; piezoelectrets; smart insole; thermoforming; wearable electronics

Academic Editors: Ahmed Abu-Siada and Dorin Petreus

Received: 28 August 2025
Revised: 9 October 2025
Accepted: 17 October 2025
Published: 30 October 2025

Citation: Amorim, M.L.M.; Ginja, G.A.; Moreira, M.d.M.A.C.; Ando Junior, O.H.; Siqueira, A.A.G.; Monteiro, V.; Afonso, J.A.; Carmo, J.P.P.d.; Afonso, J.L. Development and Evaluation of a Piezoelectret Insole for Energy Harvesting Applications. *Electronics* **2025**, *14*, 4254. https://doi.org/10.3390/electronics14214254

1. Introduction

Wearable electronic systems have rapidly evolved over the past decade, driven by the growing demand for mobile health monitoring, activity tracking, and smart footwear applications. These devices often rely on batteries, which introduce limitations related to size, weight, and the need for frequent recharging. As a result, the development of autonomous, self-powered technologies has become a crucial area of research. Among the various solutions explored, energy harvesting systems based on piezoelectric and electrostatic principles stand out due to their ability to convert mechanical movements, such as those generated during walking, into usable electrical energy. In this context, piezoelectrets have emerged as a promising class of materials, offering flexibility, low cost, and efficient charge retention for energy conversion applications in wearable devices. Piezoelectricity is the phenomenon in which certain materials generate an electric charge in response to mechanical deformation or vibration a principle discovered in 1880 by Pierre Curie. This direct piezoelectric effect is caused by the internal displacement of ions, resulting in electric polarization and a measurable electric field [1]. Conversely, when a voltage is applied, these materials undergo deformation (the reverse piezoelectric effect) [2]. Figure 1 illustrates both the direct and reverse piezoelectric effects, highlighting the conversion of mechanical deformation into electrical signal, and vice versa.

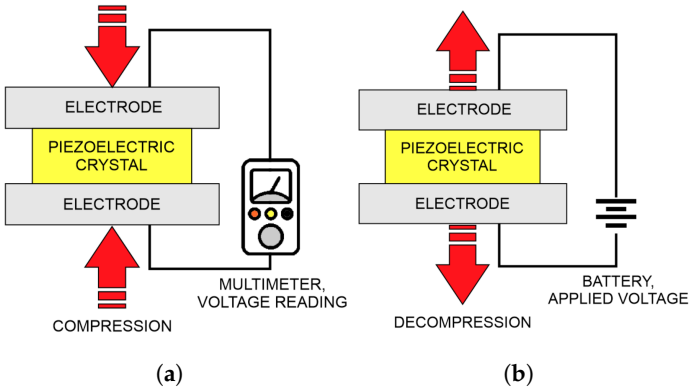

Figure 1. (**a**) Direct piezoelectric effect; (**b**) reverse piezoelectric effect.

Common piezoelectric materials include quartz, barium titanate, and lead zirconate titanate (PZT), the latter being widely used in sensors and actuators due to its strong electromechanical coupling [3–5]. Due to the potential to generate charges and, therefore, energy, studies on energy harvesting with piezoelectric sensors have emerged recently. The recent research on piezoelectric energy harvesting for self-powered systems follows several key approaches, including system frameworks, hybrid device innovation, electronic interfaces, and materials science. The goal is to power low-power electronics and Internet of Things (IoT) devices by scavenging energy from sources like human motion, environmental vibrations, and wind [6,7]. A trend involves developing hybrid systems that couple piezoelectric and electromagnetic transduction mechanisms. This approach aims to broaden operational bandwidth and improve energy conversion efficiency, with applications shown in vehicle-mounted systems for harvesting wind and vibration energy, and in devices with adjustable resonant frequencies to adapt to changing environmental conditions [8,9]. Beyond hybrid systems, research focuses on optimizing harvesters for applications involving human–machine interaction and biomechanical energy. Innovations in mechanical design include impact-driven, press-button-type harvesters that convert human actions into electrical energy [10]. The performance of these mechanical transducers, especially when subjected to aperiodic inputs from human motion, depends on the power management electronics. Consequently, harvesting circuits are an area of development, with interfaces

employing synchronous charge extraction with load-screening schemes to maximize energy from flexible thin-film generators, or Bias-Flip techniques to enable self-powered vibration sensors with high efficiency [11,12]. These electronic systems are needed to manage the high-voltage, low-current outputs of piezoelectric devices and to condition the power for storage or use. Progress in the field is also driven by fundamental materials research to find sustainable and biocompatible alternatives to lead-based piezoelectric ceramics. Work has demonstrated and quantified the piezoelectric effect in bioelectret crystal films of proteinogenic amino acids, such as L-leucine [13]. In addition to piezoelectric energy harvesters, triboelectric phenomena was also studied for the same application. An example of energy harvesting with triboelectric sensors is the development of a high-efficiency triboelectric nanogenerator (TENG) by incorporating 2D-MXene nanosheets into a PVDF-HFP tribolayer. This approach leverages an interfacial polarization strategy to enhance the material's dielectric properties and charge-trapping capability, achieving a peak power density of 4.9 W/m^2 from biomechanical energy sources such as human motion [14]. The exploration of such materials presents an avenue for creating non-toxic, biodegradable, and flexible energy harvesters and sensors. This focus on new materials, combined with advancements in hybrid device architectures and power electronics, outlines a strategy to address the challenges of efficiency, bandwidth, and material safety in kinetic energy harvesting.

Piezoelectrets or ferroelectrets are a related class of materials that function as flexible electromechanical transducers. Unlike traditional piezoceramics, piezoelectrets consist of dielectric polymer films with internal or surface charges that persist over time. These charges are typically introduced using high-voltage techniques such as corona discharge or thermal poling [15,16]. Similar to the piezoelectric sensors, electret-based energy harvesters have been studied. These systems rely on improvements in theoretical modeling and physical device architecture. Accurate prediction of device performance is essential for design, and one model for rotational harvesters improves this by incorporating three-dimensional fringing effects, achieving maximum errors of only 7.2% for Cmax and 5.9% for Cmin when compared to experimental results [17]. This model also quantifies that fringing effects can contribute up to 28.7% of the total effective capacitance, a factor often neglected [17]. On the device level, performance is frequently limited by phenomena such as squeeze-film air damping. An innovation to mitigate this is the use of a perforated electrode, which was shown to increase the maximum power output by approximately 9.8 times at a low acceleration of 2.72 m/s^2 [18]. These design strategies contribute to the broader goals in the field, such as achieving high power densities of up to 763 $\mu W/cm^3$, managing the 'pull-in' effect, and broadening the frequency bandwidth for practical applications [19].

Beyond the harvester itself, advancements in power management electronics and novel applications are extending the utility of electret technology. Efficiently extracting energy from high-impedance electret sources requires specialized electronics, such as a self-powered synchronous electric charge extraction (SECE) circuit that demonstrated a 2.15-fold increase in harvested power compared to a standard buck converter, reaching a circuit efficiency of 63% at a 5 V load [20]. The function of electret devices is also expanding to integrated systems, exemplified by a self-powered MEMS inertial switch that harvests energy from 0.3 g vibrations and triggers a wake-up signal in response to a 40 g shock [21]. Furthermore, new charging methods and materials are being explored. A micro-patterning technique using liquid-solid contact electrification achieved a surface potential of −650 V with 82% charge retention after 45 days, enabling applications in droplet-based energy harvesting [22]. The technology's scope is also expanding beyond kinetic sources with the investigation of carbon-carbon composites for thermal energy harvesting, where mild heating was found to increase the material's power density by a factor of 600 [23].

One of the defining characteristics of piezoelectrets is the presence of internal air cavities. These cavities act as regions of enhanced polarization under stress and dramatically increase the material's sensitivity to pressure. When a compressive force is applied, the distance between the charged surfaces within the cavities changes, inducing a measurable voltage. The fundamental working principle of a piezoelectret under mechanical compression is illustrated in Figure 2 shows how a piezoelectret responds to mechanical compression. The material consists of an electret layer with internal air cavities, placed between two electrodes. Figure 2a, the piezoelectret is in its uncompressed state. The internal cavities are uniformly spaced, and electric charges (positive and negative) are distributed around these cavities. The piezoelectret produces a homogenous electric field for de near area of the electrodes. Figure 2b shows the piezoelectret under compression. The applied force reduces the size of the internal cavities and brings the charges closer together. This change in geometry increases the net dipole moment, resulting in a stronger electric field and a measurable electrical signal across the electrodes.

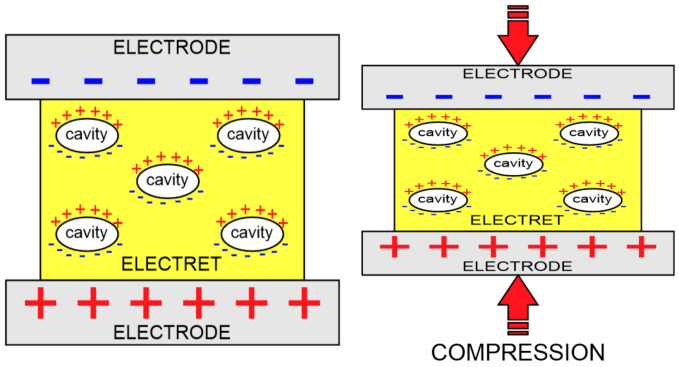

Figure 2. The effect of compression in two situations: (**a**) the piezoelectret is in its uncompressed state, (**b**) the piezoelectret is under compression.

To fabricate these structures, polymers such as PTFE or FEP are used due to their excellent dielectric strength and thermal stability. The films are thermoformed to create regular internal grooves or channels and then charged through electrostatic methods to trap charges in the cavity interfaces [24,25]. This layered configuration creates an electromechanical response that is highly suitable for energy harvesting applications, particularly in wearable systems subjected to cyclic mechanical forces like human gait. Energy harvesting from human motion has become increasingly relevant in wearable applications, where energy autonomy is critical for user comfort and system reliability. Traditional batteries are bulky and require frequent charging, which limits the practicality of fully integrated wearable devices. Piezoelectret-based systems offer a promising alternative by converting mechanical input from walking or running into electrical energy. Their low cost, high flexibility, and capability to retain charge over time make them well suited for dynamic applications such as gait monitoring, step counting, and even GPS tracking. Recent studies have demonstrated the versatility of piezoelectrets in other fields, such as acoustic sensing and fluid analysis [26,27]. However, their integration into footwear for energy harvesting is still emerging as a novel and scalable approach. Piezoelectret-based systems have demonstrated significant potential for energy harvesting and sensing applications across various configurations and fabrication methods. Single-layer and stacked piezoelectret films have been studied for vibration-based energy harvesting, achieving considerable output power enhancement proportional to the number of stacked layers, highlighting the nonlinear relationship between stress and generated power [28]. Further, advancements in geometry optimization using laser-patterned adhesive spacers have substantially

improved the piezoelectric performance, showcasing enhanced dynamic piezoelectric coefficients suitable for flexible sensor applications, including human pulse and cardiovascular monitoring [29]. Additionally, the implementation of machine learning algorithms on multifunctional piezoelectric cantilevers coated with MoS_2 (Molybdenum Disulfide) has enabled accurate simultaneous environmental sensing of parameters such as humidity, temperature, and CO_2 concentrations, demonstrating versatility and reduced complexity compared to traditional multisensor systems [30]. Fundamental insights into the manufacturing processes and properties of piezoelectrets have further underscored their high piezoelectric performance, flexibility, and diverse fabrication techniques including additive manufacturing, which expand their applicability in sensor and actuator technologies [31]. Moreover, advanced configurations and novel material modifications have been employed to enhance the sensitivity and applicability of piezoelectret devices. For instance, stacked piezoelectret microphones utilizing pressure-expanded polypropylene films achieved high sensitivities and low distortion, making them ideal for acoustic sensing applications [32]. Tape-like vibrational energy harvesters made of fluorinated polyethylene propylene (FEP) piezoelectrets exhibited notable transverse piezoelectric effects and flexibility, enabling scalable designs for wearable electronic applications [33,34]. Further material innovation was demonstrated through incorporating polydopamine-modified tourmaline nanoparticles into polyvinylidene fluoride (PVDF) matrices, significantly enhancing the piezoelectric output voltage and power density for wearable self-powered devices [35]. Finally, cross-linked polypropylene ferro/piezoelectrets have been developed into air-borne ultrasonic transducers, combining high piezoelectric activity with low acoustic impedance, thus providing improved ultrasonic emission and detection capabilities in flexible and lightweight configurations [36].

The present work is limited to proof-of-concept validation using a custom mechanical gait simulator, chosen to ensure repeatability and avoid ethical restrictions associated with early human trials. This approach enables controlled quantification of the electrical response, while laying the groundwork for subsequent in vivo testing under real gait conditions Rather than aiming for full optimization or immediate deployment, the main objective is to demonstrate the feasibility and scalability of this low-cost and passive technology as a foundational step toward developing self-powered wearable systems.

- Objective: Demonstrate the feasibility of a piezoelectret-based insole that converts human step dynamics into electrical signals suitable for future energy harvesting applications.
- Goal: Lay the groundwork for the development of self-powered wearable electronics, addressing the growing demand for energy-autonomous devices.
- Proposed Solution: A low-cost, scalable insole system using thermoformed Teflon piezoelectrets, integrated into a custom-built insole prototype.
- Sensor Placement: Piezoelectret sensors are strategically positioned in high-pressure regions such as the heel and forefoot to enhance energy conversion efficiency.
- Testing Methodology: A mechanical test rig capable of replicating human gait was developed to validate the performance of the device under repeatable and controlled laboratory conditions, as well as to avoid ethical issues related to human experimentation.
- Experimental Results:
  - The prototype generated voltage pulses exceeding 13 V under limited force (~10 kgf).
  - Average rectified DC output of approximately 3 V using a Delon circuit.
  - A parallel arrangement of eight piezoelectret elements improved signal consistency and enhanced overall energy capture.
- Theoretical Model:

  - A simplified model was developed to estimate the output voltage based on electret parameters, applied force, and the number of sensors.
  - The model aligns with experimental findings and serves as a predictive tool for future system scaling.
- Applications:
  - Potential integration into smart footwear platforms.
  - Enables future energy autonomy for low-power electronics such as fitness trackers, health monitors, and GPS modules.
- Advantages:
  - Straightforward fabrication process.
  - Use of readily available, low-cost materials.
  - Compatibility with various wearable platforms.
  - Aligned with sustainable electronics and energy harvesting trends.
- Paper Structure:
  - Section 2: Materials and methods—sensor fabrication, insole integration, test bench setup, and signal rectification circuitry.
  - Section 3: Experimental results—signal response under dynamic load, energy estimation, and model validation.
  - Section 4: Conclusion—summary of findings and their technological relevance.
  - Section 5: Future work—scaling strategies, inclusion of energy storage (e.g., supercapacitors), DC-DC converters, and integration of communication or signaling modules.

2. Materials and Methods

This section describes the complete methodology adopted for the development and experimental validation of the piezoelectret-based energy harvesting system. It begins with the fabrication of the piezoelectret sensors, detailing the materials, thermal forming process, and charging method used to achieve stable internal polarization. Following that, the mechanical integration of the sensors into a custom multilayer insole is explained, including the arrangement and connection strategy. To simulate human gait in a repeatable and controlled manner, a test rig with actuated pistons was constructed and employed in performance testing. Finally, the signal processing and rectification circuit used to convert the generated AC signals into a usable DC output is presented. Together, these methods support the experimental evaluation and theoretical modeling of the system's energy harvesting capabilities.

2.1. Fabrication of Piezoelectret Sensors

The fabrication of the piezoelectret sensors involved a sequence of mechanical, thermal, and electrical processes to obtain flexible structures with internal cavities capable of charge retention. The process began with the laser cutting of two FEP sheets (50 µm thick) and a PTFE spacer grid (100 µm thick) into 30 mm $\times$ 40 mm rectangles. The PTFE layer, patterned with a 1.5 mm pitch, defined the cavity locations. This grid was sandwiched between the FEP films and pressed at 290 °C for 10 s using a Kapton-covered thermal laminator. The steps involved in this thermoforming process are illustrated in Figure 3.

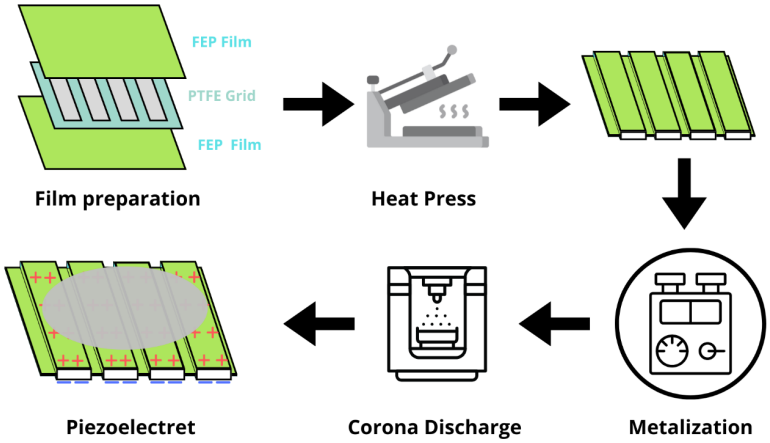

Figure 3. Steps of the preparation of the piezoelectret sensor.

The resulting cavity structures after removal of PTFE spacer can be seen in Figure 4.

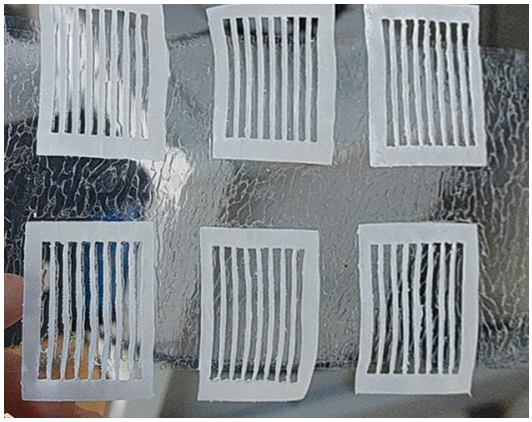

Figure 4. The result of the electret thermoforming process using the PTFE grid.

After cooling, the PTFE layer was removed, leaving air cavities between the FEP layers. The films were then metalized using a sputtering process with aluminum, applied through a mask to define circular electrode areas on both sides of the structure. Figure 5a shows the acetate masks used during sputtering, and Figure 5b displays the localized aluminum deposition on the active region.

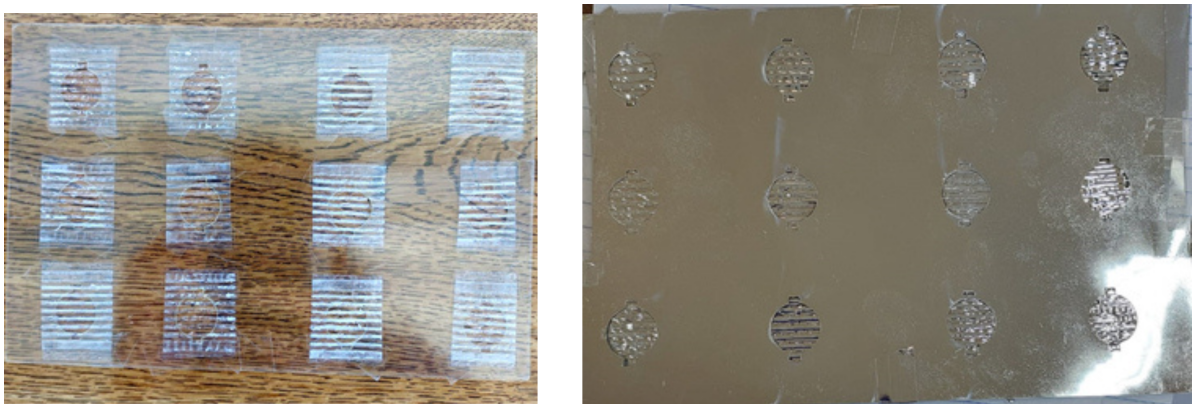

(**a**) (**b**)

Figure 5. Metalization process of piezoelectrets: (**a**) mask placement before metalization; (**b**) electrets after the sputtering process.

The electrets were charged using a 3 kV high-voltage source applied for 60 s at 25 °C, with brass and aluminum electrodes separated by ceramic insulators to ensure field concentration and safety. This method ionizes the air within the cavities, leading to stable charge trapping. The charging setup used in this stage is presented in Figure 6, which includes an adjustable top terminal and insulated base for safe operation. where (a) is the brass contact, with the positive terminal (+), (b) the electret, (c) is the aluminum negative terminal (−), (d) is the isolated ceramic base, (e) is the wheel to adjust the height of the brass contact, and (f) is the 3 kV module.

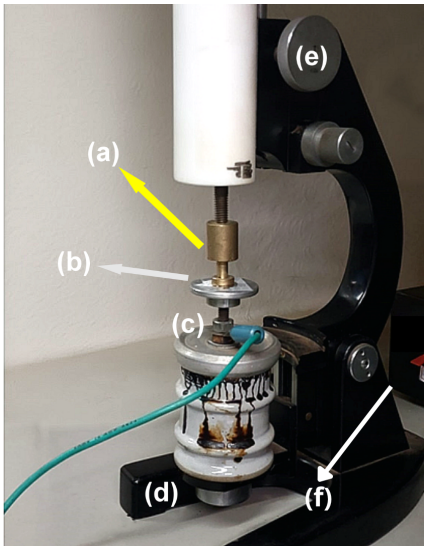

Figure 6. The charging process, (**a**) is the brass contact, with the positive terminal (+), (**b**) the electret, (**c**) is the aluminum negative terminal (−), (**d**) is the isolated ceramic base, (**e**) is the wheel to adjust the height of the brass contact, and (**f**) is the 3 kV module.

The ionization process and charge retention can be understood through Paschen's law, which describes the breakdown voltage of air between two electrodes as a function of the product of pressure (p) and distance (d):

$$V_b = \frac{Bpd}{\ln(pd) + \ln\left(\frac{A}{1+\left(\frac{1}{\gamma}\right)}\right)} \quad (1)$$

Here, A and B are empirical gas constants and γ is the secondary emission coefficient. This law is fundamental to ensure that the applied voltage ionizes the air and it charges the FEP films of the piezoelectret. Figure 7 shows the graphical representation of the Paschen's law for the air.

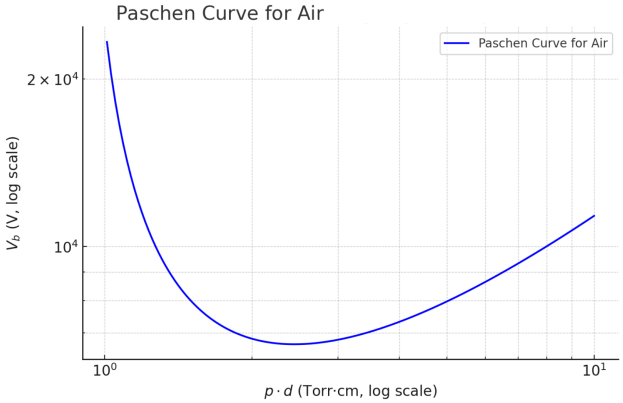

Figure 7. Graphical representation of Paschen's Law for the air. Adapted from Martins & Pinheiro [37].

With the electret structure charged, the internal electric field E between two surfaces of a single cavity can be modeled as a parallel charged capacitor and described by the following:

$$E = \frac{\sigma}{\epsilon} \tag{2}$$

where σ is the surface charge density and ϵ is the material's dielectric permittivity. These trapped electric fields allow the material to behave as a dynamic voltage generator under mechanical deformation. This multi-step fabrication process enables the production of highly sensitive, low-cost piezoelectret sensors suitable for integration into wearable systems.The Taguchi method could optimize electret fabrication by systematically testing key parameters like poling voltage, temperature, and duration in a reduced number of experiments to identify the combination that produces the most stable and highest surface charge with minimal variability [38].

Figure 8 shows the impedance of the electret measured with an Agilent E4980A LCR (Keysight, Santa Rosa, CA, USA) meter. The impedance analysis of the piezoelectret reveals a predominantly capacitive behavior, characterized by a strong inverse relationship between impedance (Z) and frequency (f). At low frequencies, specifically around 50 Hz, the device exhibits a very high impedance, exceeding 100 MΩ, indicating a strong opposition to alternating current flow. As the frequency increases, the impedance drops sharply, following the theoretical relationship for capacitive reactance, $Z \approx X_C = \frac{1}{2\pi fC}$. This behavior is consistent with an electrical model composed of a capacitor C in parallel with a large resistor R. At low frequencies, the high reactance of the capacitor causes the overall impedance to be dominated by the large parallel resistance. Conversely, at higher frequencies, the decreasing capacitive reactance provides an easier path for the current, leading to the significant drop in total impedance observed in the graph.

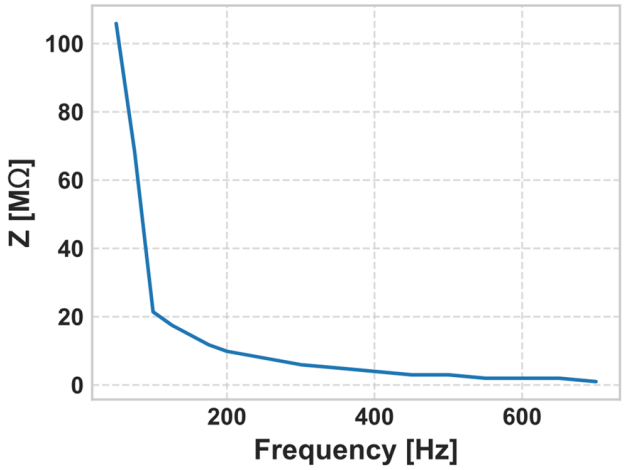

Figure 8. Impedance of the piezoelectret versus frequency.

2.2. Insole Design and Sensor Integration

To implement the energy harvesting system in a wearable format, a custom insole was developed to house the piezoelectret sensors. The insole was designed with a multilayer structure, consisting of two outer acrylic sheets (1 mm thick) and an internal rigid cardboard layer (1 mm thick) that served as both a mechanical support and cable routing plane.

The piezoelectret sensors were strategically distributed in regions of high pressure concentration during walking: the heel and the forefoot. Each of the four designated regions (two at the heel and two at the forefoot) received a pair of sensors, connected in parallel, resulting in four sensing modules. Figure 9 illustrates the anatomical placement of the sensors within the insole, aligned with known plantar pressure zones.

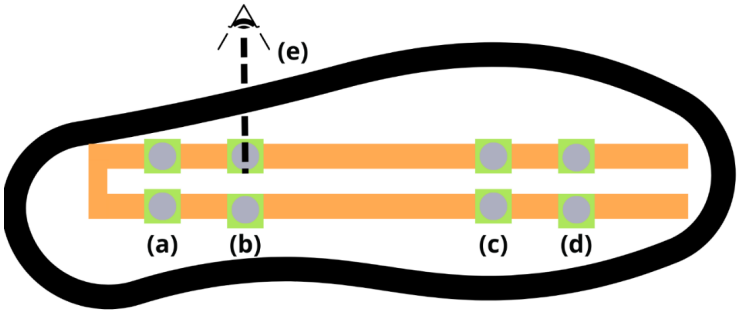

Figure 9. Piezoelectret sensors distribution in four regions: (**a**,**b**) refer to heel and (**c**,**d**) and point of view (**e**).

Each sensor module was fixed in place using adhesive copper tape, which also functioned as the electrical connection. Conductive paths were routed on both sides of the cardboard core, where the positive electrodes were linked on the upper surface and the negative electrodes on the bottom layer.

This modular parallel connection facilitated increased current output and voltage stability across the four sensing zones. Figure 9 shows a cross-sectional view of the insole layers and the embedded copper tracks for electrical continuity.

This modular parallel connection facilitated increased current output and voltage stability across the four sensing zones. Figure 10 shows a cross-sectional view of the insole layers and the embedded copper tracks for electrical continuity.

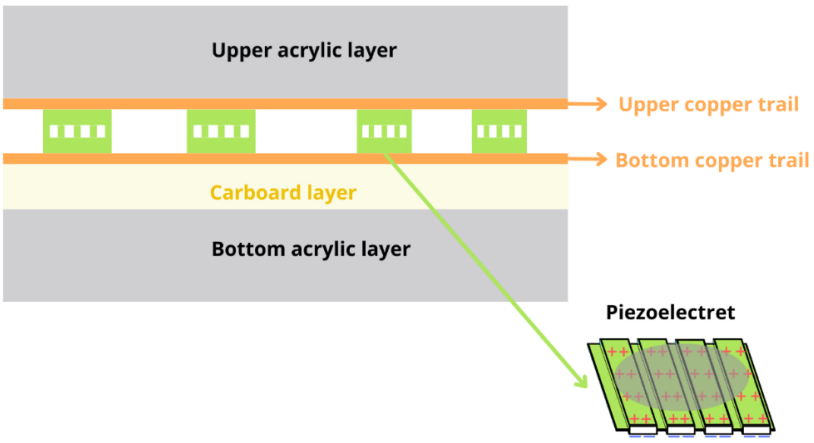

Figure 10. Cut view of the layers of the instrumented insole.

To simplify testing and validation, the output from all modules was routed to a common output terminal. Figure 11a,b presents the final assembly of the insole with the four labeled sensor zones ((a), (b), (c) and (d)), ready for integration into the mechanical test rig.

This distributed sensor layout ensured continuous signal acquisition across the gait cycle, enhancing the system's reliability under dynamic load conditions typical of real-world walking and running scenarios.

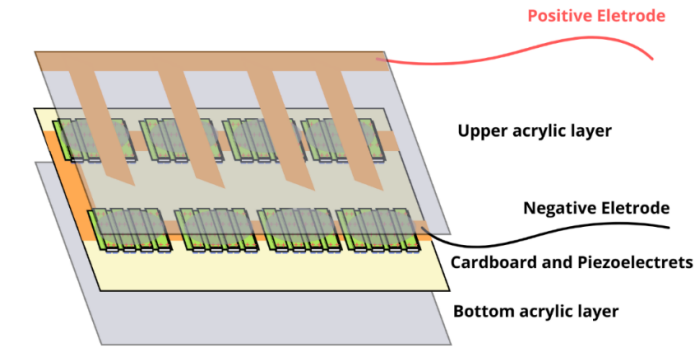

(**a**)

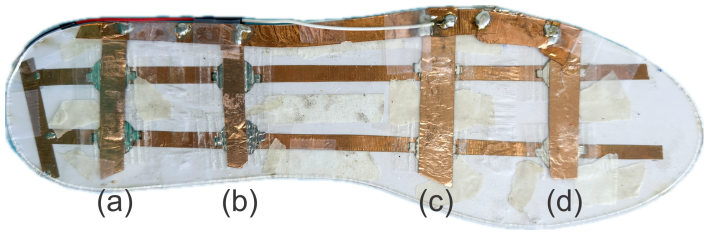

(**b**)

Figure 11. (**a**) Expanded view of the layers of the instrumented insole. (**b**) Insole instrumented with piezoelectrets in the (a) heel, (b) internal, (c) midfoot and (d) tiptoe.

2.3. Experimental Test

The human footprint during normal level walking exhibits a characteristic progression of contact, beginning at the heel, transitioning through the midfoot, and culminating at the forefoot and toes. Finite element analysis by Qian et al. (2013) demonstrated that this sequential loading pattern plays a crucial role in dynamically redistributing plantar pressure, optimizing both stability and energy transfer throughout the gait cycle [39].

This heel-to-toe motion reflects not only the biomechanical architecture of the foot but also complex neuromotor control mechanisms. Complementing this, Costa et al. (2003) applied multiscale entropy analysis to human gait and revealed that stride-to-stride variability particularly in this posterior-to-anterior shift of the footprint is governed by nonlinear dynamics, reflecting the adaptability and complexity of locomotor control [40]. Together, these findings underscore the importance of temporal and spatial coordination in the natural progression of plantar contact during walking. In order to ensure full control over the experimental tests and achieve consistent repeatability while minimizing human error and imprecise foot strikes, and avoiding the evaluation of electrical performance under uncontrolled dynamic loading conditions. A custom experimental test rig was developed. This system was designed to simulate the compressive forces applied during human gait in a repeatable and controlled laboratory environment. providing a precise measurement. The test bench consisted of four vertical solenoid pistons, each capable of applying up to 25 N of force, corresponding to approximately 2.5 kgf. These pistons were precisely aligned with the sensor zones of the insole, enabling localized compression that mimics heel and forefoot contact during walking or running. this represents a fraction of the ideal force generated but on a controlled enviroment because during normal level walking, the vertical ground reaction force (vGRF) typically ranges from 1.0 to 1.5 times the individual's body weight, and can reach up to 2.0 to 3 times body weight during running. For a person weighing 70 kg (686 N), this corresponds to approximately 700–1050 N (70–105 kgf) during walking, and up to 1370–2000 N (137–200 kgf) when running. These values are reported

in biomechanical studies of gait dynamics, such as by Keller et al. (1996), which analyzed impact forces during locomotion [41]. Figure 12 depicts the gait cycle phases.

Figure 12. Human walking gait cycle.

Figure 13 shows the schematic of the solenoid-driven test rig used to simulate human gait. (a) Pistons in the force-application state (red arrows), mimicking the stance phase when the foot presses the insole. (b) Pistons in the released state (blue arrows), corresponding to the swing phase when the foot is lifted. (c) Yellow bar represents the instrumented insole. (d) Rectangular blocks represent the solenoid pistons. This configuration reproduces the sequential heel-to-toe compression pattern of human walking in a controlled and repeatable laboratory setup.

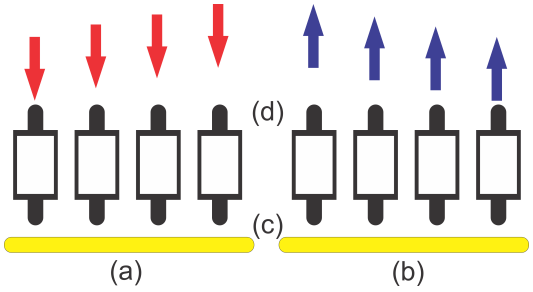

Figure 13. Ovement of the solenoid pistons used to simulate human gait. (**a**) Pistons applying downward force (red arrows), reproducing the stance phase when the foot presses the insole. (**b**) Pistons in the released position (blue arrows), corresponding to the swing phase when the foot is lifted. (**c**) The yellow bar represents the instrumented insole. (**d**) Rectangular blocks represent the solenoid pistons.

Figure 14 shows the complete experimental test rig developed to simulate human footstep patterns in a controlled environment. This custom-built footprint simulator reproduces the sequential heel-to-toe loading cycle observed during human gait, with precise control of timing and force application. (a) indicates the instrumented insole mounted on the test bench, where compressive forces are applied to the piezoelectret sensors. (b) is the bridge holding the four vertical solenoid pistons (model JF1039), each capable of generating approximately 25 N of force, which reproduce localized plantar pressure during the contact phases. These pistons are actuated with short pulses of approximately 1.5 ms to replicate the transient impact characteristic of human heel strike, and the system supports step frequencies up to 5 Hz, corresponding to a running speed of about 22 km/h. (c) shows the custom power stage, based on MOSFET switching with an aluminum heatsink for thermal management, driven by an ATmega328PB microcontroller (Microchip, Chandler, AZ, USA) that manages the activation sequence and basic parameters of the solenoids. (d) corresponds to the higher-level control unit, based on an ESP32, which allows fine-tuning of operational variables such as frequency, delay, and duty cycle through user-adjustable potentiometers. (e) highlights the guided spindle-lifter mechanism that ensures accurate vertical alignment of the solenoids, while (f) is the stepper motor that actuates the lead

screw, maintaining platform positioning and providing stable mechanical support during the tests. Together, these subsystems enable a high-fidelity and repeatable simulation platform that bridges laboratory testing with real-world gait mechanics.

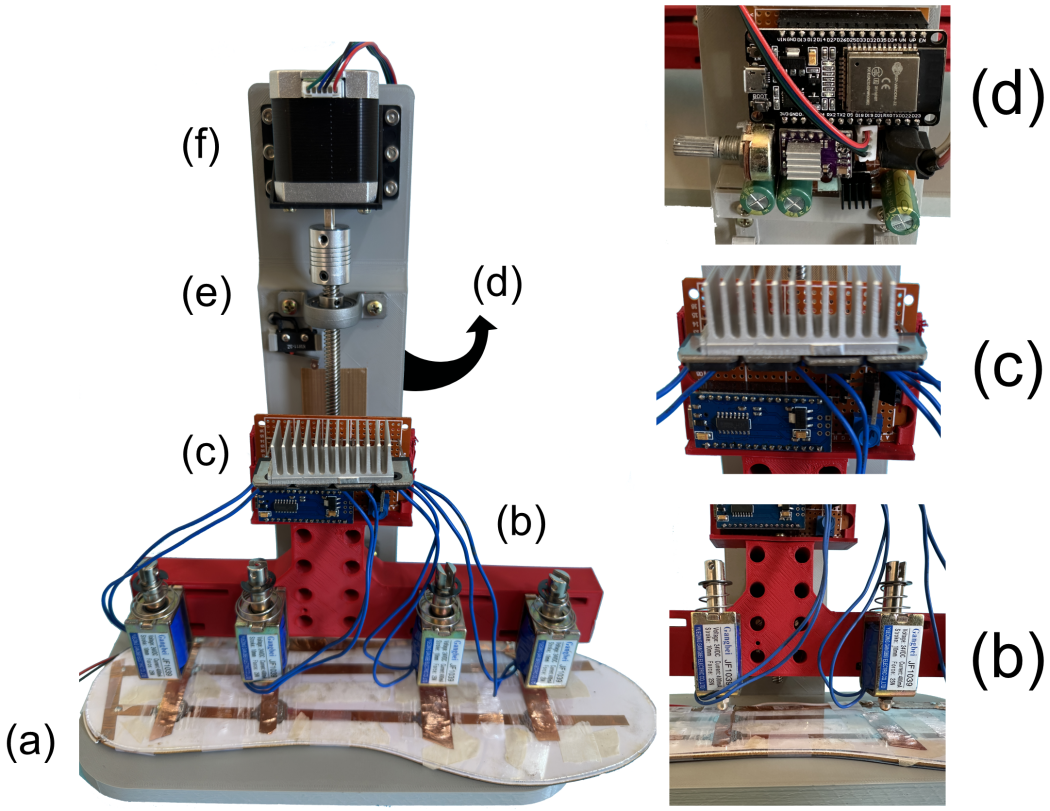

Figure 14. Experimental test rig developed for controlled gait simulation. (**a**) Instrumented insole with piezoelectret sensors mounted on the test bench. (**b**) Bridge with four linear solenoid pistons (JF1039, 25 N each) for localized compression. (**c**) Custom MOSFET driver stage with heatsink and ATmega328PB microcontroller for solenoid activation. (**d**) ESP32-based control unit with potentiometers for fine-tuning operational parameters. (**e**) Guided spindle-lifter mechanism ensuring vertical alignment of the pistons. (**f**) Stepper motor driving the lead screw to maintain platform positioning and provide stable support during testing.

This experimental platform provided a reliable, repeatable way to evaluate the electrical response of the insole system under controlled mechanical loads, paving the way for quantitative performance analysis and model validation.

2.4. Electrical Circuit and Signal Rectification

The piezoelectret sensors embedded in the insole generate alternating voltage signals (AC) in response to mechanical compression during the simulated gait cycle. To convert these signals into a usable direct current (DC) output for potential energy harvesting applications, a passive rectification circuit was implemented. The selected topology was a Delon voltage doubler circuit, also known as a peak detector, composed of two 1N5408 diodes and two 1 nF ceramic capacitors. In theory, this configuration can both rectify and double the peak voltage of an AC signal. However, due to the specific electrical characteristics of the piezoelectret source such as high internal impedance, low output current, and low-frequency content, the circuit behaved primarily as a half-wave rectifier, failing to achieve effective voltage doubling under dynamic load conditions. This behavior is consistent with the limited charge transfer observed during the negative half-cycle, which was insufficient to fully charge the second capacitor. Despite this, the use of the Delon topology was motivated by several practical considerations. Its simplicity and low

component count make it a cost-effective and compact solution for low-power systems. Additionally, it is well-suited for signals with low amplitude and high impedance, where more complex active converters (e.g., buck or boost regulators) would be inefficient or unnecessarily complex. Most importantly, the goal of this setup was not to maximize harvested energy, but rather to characterize the electrical behavior of the piezoelectret sensor under dynamic mechanical loading. In this context, the Delon circuit still provided a stable and filtered DC output, enabling reliable oscilloscope measurements of waveform shape, peak amplitude, and average voltage [42–45]. Figure 15 illustrates the implemented circuit, where (a) represents the insole acting as an AC voltage source, (b) the connecting wires, and the two diodes perform the rectification stage. The capacitors alternate charge storage over each half-cycle. The output voltage was measured at point (c) using an oscilloscope, while (d) a load resistor of 10 kΩ was selected as a representative value commonly used in energy-harvesting characterization studies. This resistance provides a current draw in the hundreds of microamperes for voltages in the range of 1–3 V, consistent with the consumption levels of ultra-low-power wearable devices and sensor front-ends. Moreover, it represents a practical compromise: sufficiently low to emulate a realistic load, yet high enough to avoid excessive damping of the piezoelectret output during testing. In summary, although the Delon circuit did not perform as a voltage doubler in this specific case, it still offered effective signal rectification and filtering, meeting the experimental requirements for sensor evaluation in a simple and efficient manner.

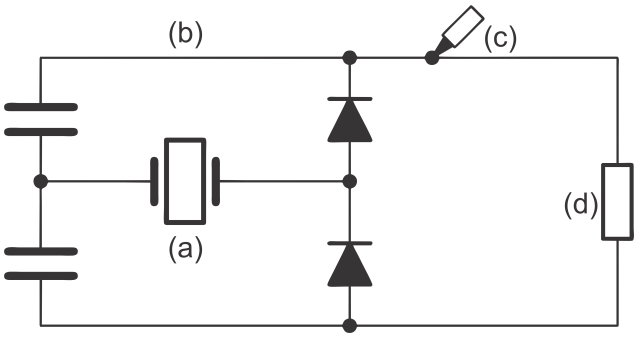

Figure 15. Delon voltage multiplier circuit, (**a**) insole, provide AC voltage. (**b**) Wires connects the insole to the rest of the voltage multiplier stage. Two diodes do the rectifying stage. Two capacitors store charge during different parts of the AC cycle. (**c**) Oscilloscope probe: this point in the circuit is where the output voltage is measured using an oscilloscope. (**d**) Load resistor: this represents the load connected to the voltage multiplier, in this case, a 10 kΩ.

3. Results

This section presents the experimental results obtained from the piezoelectret-based energy harvesting system and discusses their implications in terms of signal consistency, energy conversion, and theoretical validation. The performance of the insole was analyzed under dynamic loading using the test rig described in the previous section. The electrical outputs generated by the sensors were examined in both time and frequency domains, and key metrics such as peak voltage, pulse duration, and average DC output were measured. These results are further interpreted through a simplified theoretical model that establishes a linear relationship between the applied force and the generated voltage. Using the test rig as a controlled stepping analog allowed the experiments to be highly consistent, precise, and repeatable. Each solenoid piston applied a force of 25 Newtons (N) to the insole surface. To relate this to human step dynamics, the applied force must be converted into kilogram-force (kgf), a more intuitive unit for representing body weight distribution.

Thus, the equivalent force produced by each piston in kgf can be calculated using the following equation.

$$Force(\text{kgf}) = \frac{Force(N)}{9.80665} \approx 2.5\,\text{kgf} \tag{3}$$

This force value closely resembles the pressure applied by a partial footstep, making the test conditions suitable for simulating realistic gait-related impacts. The test rig employs four pistons, which produce a combined total of approximately 10 kgf. In comparison, a 70 kg person walking usually exerts about 70 kgf per step, equivalent to their body weight. When running, as previously mentioned, the same person can generate between 2.3 and 3 times more force, resulting in an impact force ranging from 173 kgf to 214 kgf per step. Therefore, the total force applied by the pistons in this setup represents only a fraction of the mechanical energy that the electrets would be exposed to under real human motion. Despite the reduced input, the electrets were still able to generate measurable electrical signals.

3.1. Electrical Output and Signal Analysis

The electrical response of the insole under dynamic mechanical excitation was evaluated using the solenoid-based test rig operating at a frequency of four steps per second, which corresponds to a simulated running speed of approximately 20 km/h, assuming an average stride length of 1.4 m. Each actuation event applied a compressive force to the piezoelectret sensor zones, resulting in distinct voltage pulses characterized by sharp rise and fall transitions, consistent with the dynamic nature of heel–toe contact. To assess signal integrity and reliability over time, extended testing was performed for a total duration of 25 min, during which periodic waveform samples were recorded. Figure 16 shows the electrical response of a single pulse.

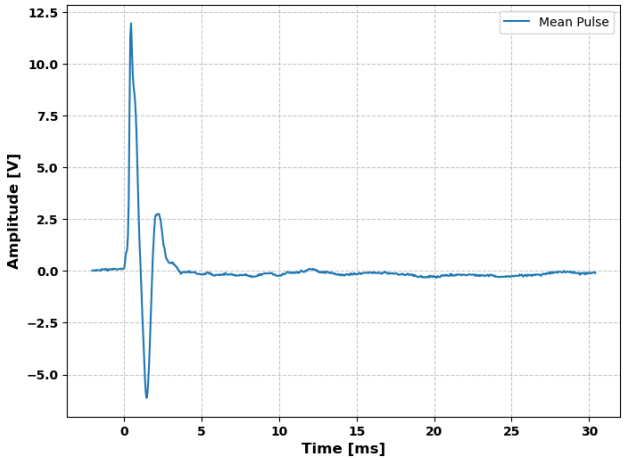

Figure 16. Single pulse generated by the insole.

Figure 17 presents a detailed view of the typical voltage waveform generated by a single piezoelectret module subjected to a compressive force of 25 N. The pulse exhibits a sharp rising edge followed by a damped oscillatory decay, reaching a peak amplitude of approximately 13 V. The total pulse duration is around 6 milliseconds, corresponding to the transient mechanical compression imposed by the solenoid actuator. This waveform illustrates the fast electromechanical response of the piezoelectret structure and confirms its ability to transduce rapid dynamic loads into measurable electrical signals with high sensitivity and temporal resolution.

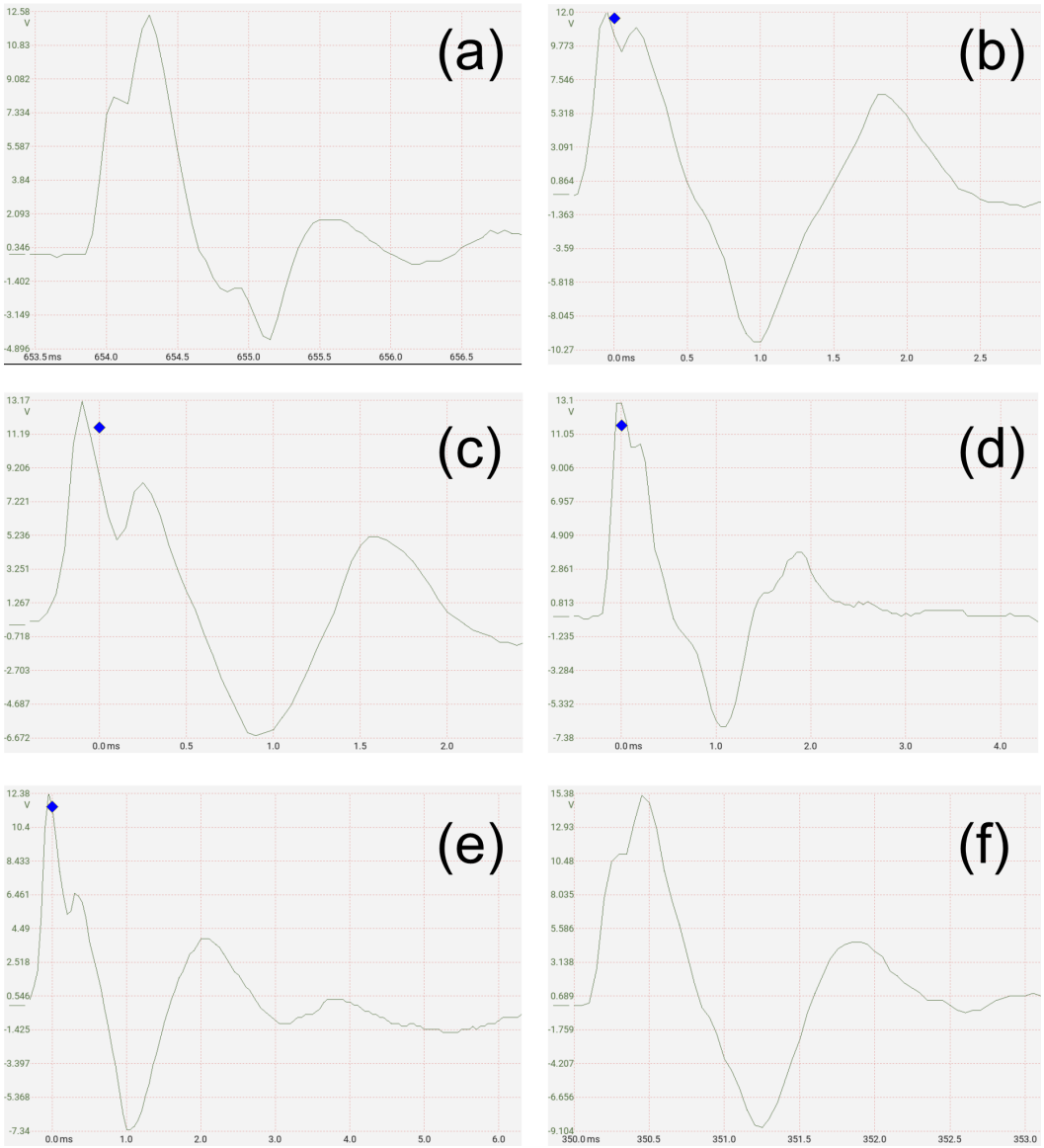

Figure 17. Presents representative oscilloscope traces acquired at six time intervals: (**a**) initial time (0 min), (**b**) 5 min, (**c**) 10 min, (**d**) 15 min, (**e**) 20 min, and (**f**) 25 min.

In order to extend the electromechanical characterization of the piezoelectret response, additional performance metrics were estimated from the measured voltage waveform and the capacitor-based model of the sensor. The instantaneous charge Q transferred during a compression cycle can be expressed as follows:

$$Q = C \cdot \Delta V \tag{4}$$

where C is the effective capacitance of the piezoelectret element and ΔV is the peak voltage variation during the pulse. Normalizing this charge by the active electrode area A, the surface charge density σ is obtained as follows:

$$\sigma = \frac{Q}{A} \tag{5}$$

which provides an indicator of the trapped charge effectiveness in the electret structure.

The corresponding peak current I_{peak} is given by the derivative of the voltage across the capacitor as folows:

$$I_{peak} = C \cdot \frac{dV}{dt} \tag{6}$$

Its normalized value yields the current density J as follows:

$$J = \frac{I_{peak}}{A}. \tag{7}$$

The harvested energy per compression event can be approximated by the stored energy in the equivalent capacitor as follows:

$$E = \frac{1}{2} C \cdot (\Delta V)^2. \tag{8}$$

Finally, dividing this energy by the active volume V_{act} of the sensor leads to the energy density ρ_E:

$$\rho_E = \frac{E}{V_{act}}. \tag{9}$$

These metrics charge density, current density, and energy density provide a more complete description of the electromechanical conversion process and enable fair comparison with other energy harvesters reported in the literature.

Quantitative Metrics from the Typical Pulse

From the representative waveform in Figure 15, the following measurable quantities can be extracted with oscilloscope cursors: (i) peak amplitude V_{peak}, (ii) pulse width τ (e.g., full width at half maximum, FWHM), (iii) rise time t_r (10–90%), (iv) fall time t_f, (v) inter-pulse period T (or step frequency $f = 1/T$), and (vi) ring-down frequency f_d and decay envelope (for damping/quality factor).

A conservative RMS estimate of a narrow pulse train can be obtained under a rectangular approximation:

$$V_{\text{RMS}} \approx V_{\text{peak}} \sqrt{\frac{\tau}{T}}, \tag{10}$$

which provides a lower-bound normalization for comparison across operating conditions.

Given the equivalent capacitive model of the piezoelectret element, additional electrical figures of merit can be derived once the effective capacitance C and active electrode area A are known/estimated:
Transferred charge per pulse

$$Q = \int I(t)\, dt \approx C\, \Delta V, \tag{11}$$

where ΔV is the pulse excursion (typically $\Delta V \simeq V_{\text{peak}}$ for an open-circuit snapshot).
Surface charge density

$$\sigma = \frac{Q}{A} \approx \frac{C\, \Delta V}{A}. \tag{12}$$

Peak current and current density

$$I_{\text{peak}} = C \left.\frac{dV}{dt}\right|_{\text{rise}}, \qquad J_{\text{peak}} = \frac{I_{\text{peak}}}{A}. \tag{13}$$

In practice, $\left.\frac{dV}{dt}\right|_{\text{rise}}$ can be estimated from the 10–90% rise segment as $\left.\frac{dV}{dt}\right|_{\text{rise}} \approx 0.8\, V_{\text{peak}}/t_r$.

Energy per compression event and energy density

$$E = \frac{1}{2} C (\Delta V)^2, \qquad \rho_E^{(\text{area})} = \frac{E}{A}, \qquad \rho_E^{(\text{vol})} = \frac{E}{V_{\text{act}}}, \tag{14}$$

where V_{act} is the active volume of the transduction region.
Average power (per channel) at repetition rate f

$$\overline{P} = E \cdot f. \tag{15}$$

Together, these directly measurable (or single-parameter-derived) metrics—V_{peak}, τ, t_r, t_f, f, f_d, Q, σ, J_{peak}, E, ρ_E, and $\overline{P}$ provide a compact yet comprehensive description of the electromechanical response and enable comparison with prior energy harvesters.

Figure 17 presents representative oscilloscope traces acquired at six time intervals: (a) initial time (0 min), (b) 5 min, (c) 10 min, (d) 15 min, (e) 20 min, and (f) 25 min. The results demonstrate a stable signal profile with negligible degradation in voltage amplitude, waveform shape, or response time, indicating that the electrodes retained their ability to convert mechanical impact into electrical output throughout the entire test duration. This confirms the electromechanical reliability and repeatability of the insole system under sustained dynamic loading conditions.

The waveform features a rapid rise time, indicating an immediate electromechanical response, followed by a symmetrical decay. The positive part of the pulse is due to the approximation of the parallel films of the tubular channels and the symmetrical decay is the reverse polarization due to the return of the original state of the films after the force is released. The signal is highly repeatable, as confirmed by the persistence mode on the oscilloscope, which overlays multiple cycles without significant deviation. This repeatability is crucial for practical energy harvesting systems, as it ensures a stable power supply and facilitates modeling. Furthermore, the well-defined pulse shape enables precise estimation of instantaneous power and energy per cycle. Figure 18 shows a sequence of pulses recorded over a 1 s interval, highlighting the periodicity and consistency of the output when subjected to cyclic loading conditions.

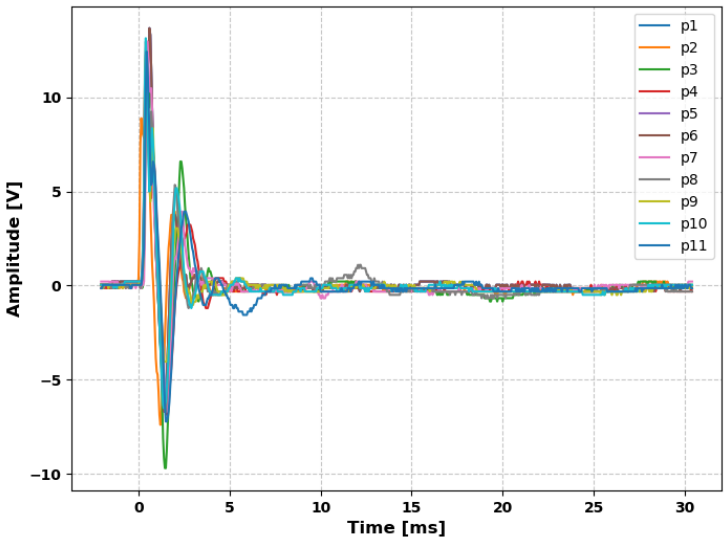

Figure 18. Response of the 11 generated pulses.

In order to reassure the repeatability of the generated pulses of the piezoelectret insole, the mean and standard deviation values for all pulses was calculated and is shown in Figure 19.

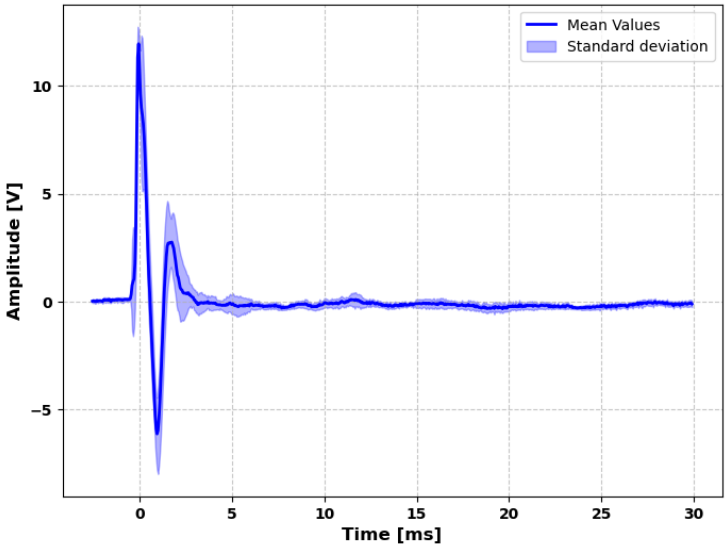

Figure 19. Mean and standard deviation for all the generated pulses.

3.2. Harvested Energy Estimation

The time-domain behavior of the piezoelectret system was evaluated to assess its performance under different frequencies simulating walking and running.

At a frequency increased to 5 steps per second, corresponding to a simulated speed of approximately 22 km/h, the generated signal exhibited consistent timing between pulses, with uniform peak intervals and no delay-induced degradation.

The reliability of pulse timing is critical in applications where energy storage or power management circuits depend on predictable input behavior. This consistency also facilitates synchronization with other wearable system modules.

To properly quantify the level of energy harvested during the tests, the AC pulses generated by the piezoelectrets must be converted into an equivalent DC voltage. This can be estimated using the RMS value of the pulse signal which measures the equivalent of the average power of an AC signal [46]. The RMS value V_{RMS} is determined by the following:

$$V_{RMS} = \frac{1}{T}\sqrt{\int_0^T [v(t)]^2 dt} \tag{16}$$

where:

- V_{RMS}: is the RMS output voltage;
- $v(t)$ is the time-varying pulse signal;
- T: is the period of the signal (30 ms).

By applying this method to the mean value of the measured pulses, an RMS voltage of approximately 3 V was obtained. This value represents the effective energy contribution of each dynamic event over time, converting the alternating electrical behavior of the piezoelectret into a steady-state DC equivalent suitable for energy storage or powering low-power electronic devices. Figure 20 illustrates this relationship, showing the repetition of representative AC voltage pulses generated at 5 steps per second (blue waveform), overlaid with a constant orange line representing the calculated RMS voltage. This RMS line reflects the equivalent DC value that would deliver the same amount of energy over time, allowing a direct comparison between transient piezoelectric signals and their potential in real-world energy harvesting applications.

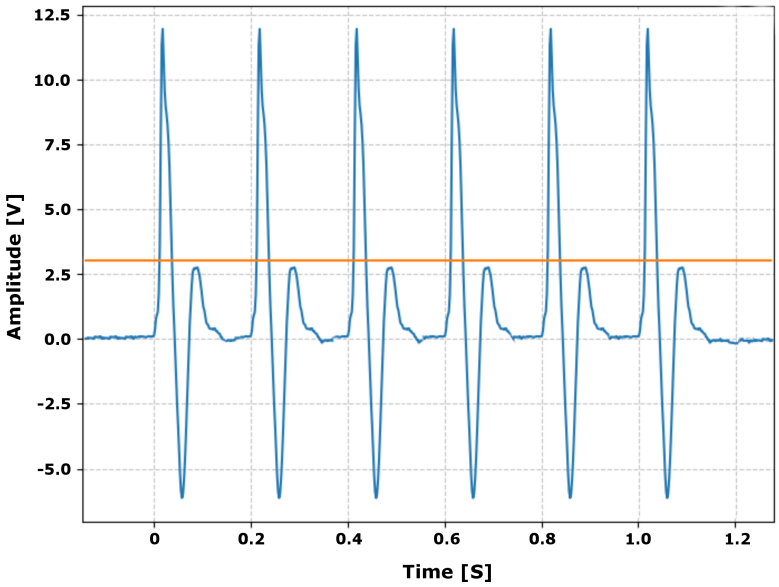

Figure 20. Equivalency between AC peaks in blue and 3V DC RMS.

In addition to voltage analysis, the system's average current output under a 10 kΩ resistive load was estimated to assess its energy delivery capacity. Given the DC-equivalent voltage V of approximately 3 V, the resulting current I is as follows:

$$I = \frac{V}{R} = \frac{3\ \text{V}}{10\ \Omega} = 300\ \mu\text{A} \tag{17}$$

This corresponds to an average power output of the following:

$$P = V.I = 3\ \text{V}.300\ \mu\text{A} = 900\ \mu\text{W} \tag{18}$$

This power output is a result of the individual contribution of the eight piezoelectrets, yielding an effective contribution of 112.2 µW per sensor. While modest, this power level is compatible with intermittent operation of ultra-low-power systems such as signaling LEDs or Bluetooth Low Energy (BLE) modules. These results confirm the practical viability of the energy harvesting strategy for powering discrete embedded devices in wearable electronics.

To provide a normalized perspective of the harvester's performance, the measured average power of 900 µW was divided by the active sensor area of 76.8 cm^2 (eight sensors of 30 × 40 mm each). This yields a power density of approximately the following:

$$P_d \approx \frac{900\ \mu\text{W}}{76.8\ \text{cm}^2} \approx 11.7\ \mu\text{W/cm}^2.$$

Similarly, the average current of 300 µA results in a current density of the following:

$$J_d \approx \frac{300\ \mu\text{A}}{76.8\ \text{cm}^2} \approx 3.9\ \mu\text{A/cm}^2.$$

These normalized figures allow a direct comparison with state-of-the-art piezoelectric and triboelectric energy harvesters, and confirm that the proposed insole operates within the expected range for polymer-based devices.

3.3. Theoretical Modeling of the Energy Harvesting Mechanism

To provide analytical insight into the behavior of the piezoelectret-based energy harvesting system, a simplified physical model is proposed. Each electret unit is approximated as a parallel-plate capacitor, in which the electrodes are separated by a distance d, and the

electric field is generated by permanently trapped charges on the internal surfaces. As seen in Figure 21.

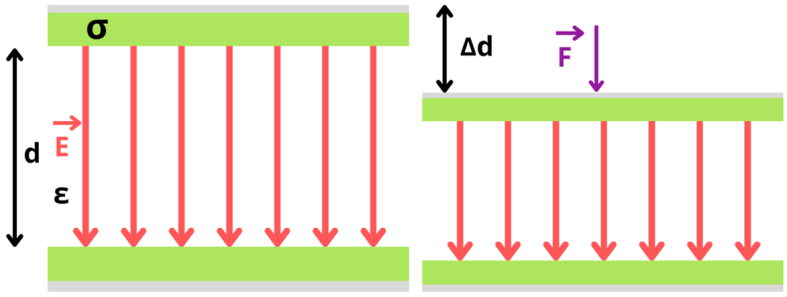

Figure 21. Behavior of the piezoelectret-based energy harvesting system.

Assuming a uniform surface charge density σ and dielectric permittivity ϵ, the electric field E between the plates is given by the following:

$$|\vec{E}| = \frac{\sigma}{\epsilon} \tag{19}$$

When the structure is mechanically compressed, the distance between the plates decreases by a small amount Δd. Under the assumption that the internal electric field remains approximately constant during this small deformation, the resulting change in voltage ΔV across the electret can be approximated by the following:

$$\Delta V = E.\Delta d = \frac{\sigma}{\epsilon}.\Delta d \tag{20}$$

The displacement Δd is related to the applied force F through Hooke's Law, assuming linear elastic behavior, is as follows:

$$\Delta d = \frac{F}{A.Y} \tag{21}$$

where A is the electrode area and Y is the Young's modulus of the dielectric material. Substituting into Equation (8), we obtain the following:

$$\Delta V = \frac{\sigma.F}{\epsilon.A.Y} \tag{22}$$

This expression shows that the generated voltage is linearly proportional to the applied force. For an array of X identical electrets connected in parallel, the overall voltage output remains the same, but the current capacity increases. However, for modeling purposes, we define a practical proportionality constant for the insole configuration:

$$\kappa_{insole} = \frac{\Delta V_{Insole}}{X.F} \tag{23}$$

This constant can be calculated based on the experimental data. For example, considering a measured voltage of 260 mV from eight sensors under a total force of 25 N, we obtain the following:

$$\kappa_{insole} = \frac{3\text{V}}{8.25\,\text{N}} = 15\,\text{mV/N} \tag{24}$$

This result suggests that, on average, each Newton of applied force generates approximately 15 mV per electret module, which aligns well with the experimental voltage pulses observed in Section 3.3. The model, despite simplifications, provides a useful predictive tool for system scaling and optimization in future designs.

It is important to note that the present setup applied approximately 25 N per piston, corresponding to localized loading of each insole zone. This choice ensured that the piezoelectret films operated within the small-strain elastic regime, avoiding nonlinear or saturation effects while still producing measurable and repeatable signals. Since the voltage output scales linearly with the applied force under these conditions, the measured response can be extrapolated to realistic ground-reaction forces of 700–1000 N observed during human gait. In this scenario, the load is distributed among multiple zones of the foot, and the harvested energy per step increases quadratically with force:

$$E \propto F^2 \qquad \text{with} \qquad E = \tfrac{1}{2} C\,(\Delta V)^2. \tag{25}$$

Thus, the experimental operating point at 25 N per piston provides a valid basis for scaling toward real-use conditions while maintaining linearity and material integrity.

3.4. Piezoelectret Insole Benchmark

In order to evaluate the response of the piezoelectret insole, Table 1 shows a comparative between the results of the piezoelectret insole compared to other energy harvesting systems.

Table 1. Comparison between this work and other energy harvesting methods.

Harvesting Method	Generated Output	Reference
Piezoelectric Button	190 µJ / impact	[10]
MEMS Vibrational EHs	1.548 µW / m/s^2	[18]
Self-Powered MEMS Electret	380 nW/g (peak)	[20]
Triboelectic nanogenerator	4.9 W/m^2 (peak)	[14]
Tubular FEP Piezoelectret Insole	90 µW/kgf or 15 mV/N (mean)	This Work

The piezoelectret insole demonstrates a feasible and scalable approach to biomechanical energy harvesting, achieving notable voltage outputs from a low-cost, flexible platform. Under a controlled, limited-force load of approximately 10 kgf, the system consistently generated voltage peaks up to 13 V, with an estimated average power output of 900 µW. The key achievement of this work is the validation of a simple and scalable fabrication process using thermoformed Teflon films, positioning the technology as a practical solution for integration into smart footwear. When benchmarked against other energy harvesting technologies, the performance of the piezoelectret insole is best understood by the application and transduction method. Its power output is modest when compared to other footstep-based harvesters; for example, mechanical systems using fluid-flow have reported significantly higher average power, reaching up to 1.4 W per step. This highlights that while piezoelectrets offer simplicity, other mechanical methods can capture a larger fraction of the available energy. In the realm of advanced materials, triboelectric nanogenerators (TENGs) show exceptionally high peak power density (4.9 W/m^2), indicating superior efficiency per unit area. Similarly, devices designed for discrete, high-force events, like a piezoelectric press-button harvester, can produce much higher instantaneous power (20 mW per impact). In the broader context of vibration energy harvesting, the insole's output is lower than that of systems targeting more consistent or powerful sources. Hybrid systems for wind energy can generate over 46 mW, and devices tuned for specific resonant machine vibrations can yield 9.1 mW. However, the insole's power generation is substantially greater than that of miniaturized MEMS-based harvesters, which operate in the microwatt and nanowatt range. In conclusion, while the insole's 900 µW output is not the highest, its primary advantages are its low cost, simplicity, and scalability. This positions it as a practical solution for powering low-consumption wearable electronics, such as simple sensors or BLE modules, rather than as a high-power source.

To advance this technology toward real-world use, future efforts will focus on resolving key challenges in scalability and environmental resilience. For scalability, the straightforward thermoforming process is highly amenable to automated manufacturing techniques, where precise control over temperature and pressure can ensure high manufacturing uniformity across all sensors, leading to predictable and reliable energy output in a full-coverage insole. Regarding long-term durability, the inherent mechanical resilience of the FEP and PTFE films is a significant advantage, and this can be further enhanced with advanced encapsulation methods that protect the internal structures from material fatigue. According to the manufacturer, the FEP film is durable for at least 10,000 cycles to a maximum 31 MPa stress [47]. To ensure stable performance against environmental factors like humidity or sweat, the current multi-layer design already offers physical protection. This protection can be augmented with hermetic sealing or hydrophobic coatings to prevent moisture ingress, thereby preserving the stable charge retention and ensuring the integrity of the output signals. By addressing these factors, the system's robustness can be fully realized for commercial smart footwear applications.

It should be noted that the present validation was performed exclusively under controlled conditions using a mechanical gait simulator. While this approach ensured repeatability and isolation of electrical performance, it does not fully replicate the variability of human gait. Therefore, real-time insole application testing with human participants will be a necessary step to validate durability, comfort, and energy yield under realistic biomechanical conditions.

4. Conclusions

The results presented in this work confirm that the proposed methodology for integrating piezoelectret-based energy harvesting systems into footwear is both functional and highly scalable. The custom insole, equipped with eight piezoelectret sensors positioned at high-impact regions (heel and forefoot), successfully converted simulated step loads into measurable electrical energy, validating the viability of the system.

Controlled testing using a solenoid-driven rig enabled consistent evaluation of electrical output under repeatable gait conditions. The sensors produced voltage pulses ranging from 5 V to over 13 V under low-force scenarios (10 kgf), with pulse durations above 1 ms. These levels are sufficient to activate low-power electronic circuits. The entire system was fabricated using cost-effective methods including laser-cut FEP/PTFE layers, thermal lamination, and aluminum sputtering making it suitable for large-scale and low-cost production.

The mean value of all collected pulses was used in order to evaluate the capability of the sensor to transduce force into energy. The calculated RMS output of the generated pulse was approximately 3 V and the estimated power was 900 µW. In a real-life environment, a human walk would lead to greater forces applied to the insole and, therefore, a greater generated energy. The resulting voltage could be sufficient to power low-energy embedded systems embedded in footwear. Such systems may include fitness trackers, GPS modules, step counters, or other wearable electronics, enabling self-powered smart shoes for health monitoring, sports performance, or personal safety applications [48–50].

From a scalability perspective, the current design utilizes only a portion of the available insole area. Even so, it produced usable energy levels, suggesting that a full-coverage configuration could significantly increase energy yield per step. This opens the door to powering embedded systems such as GPS modules, fitness trackers, health monitors, or wireless communication devices within a self-powered smart shoe. The potential applications of this technology extend beyond footwear. The concept of harvesting mechanical energy from motion is applicable to prosthetics, industrial vibration sensing, biomedical monitoring,

and other wearable systems that benefit from autonomous power sources. In conclusion, the proposed system is technically robust, economically viable, and easily replicable. Its simplicity, low cost, and adaptability position it as a compelling solution for sustainable energy harvesting in the next generation of intelligent wearable electronics.

5. Future Work

Future developments of this research aim to expand the active surface area of the piezoelectret elements to enhance energy harvesting efficiency under gait-induced mechanical loading. Increasing the physical dimensions of the electret layers or employing a larger number of sensors is expected to significantly boost charge displacement and improve voltage generation under realistic plantar pressure profiles. In addition, optimization of fabrication parameters, such as thermal pressing conditions and electrode geometry, may further enhance device performance. From a system integration perspective, a custom low-input-voltage boost converter is currently under design, together with fast-charging supercapacitors that will serve as energy buffers, enabling stable output to power ultra-low-power devices such as indicator LEDs, Bluetooth Low Energy (BLE) beacons, or GPS trackers. Together, these improvements are expected to transform the current prototype into a fully autonomous and robust energy-harvesting platform.

Beyond these aspects, future work will also address experimental durability tests, extending up to several hundred thousand gait cycles, to quantify long-term stability and fatigue resistance of the piezoelectret films under repetitive stress. Additional figures of merit, such as experimentally measured energy density and surface charge density, will be incorporated to enable rigorous benchmarking against state-of-the-art harvesters. Importantly, in vivo testing with human participants will be carried out under different gait conditions (walking, running, stair climbing) to validate electrical performance under realistic biomechanical variability. Finally, ergonomic evaluations of thickness, flexibility, and comfort will be performed to ensure the suitability of the insole for prolonged daily use, consolidating its potential for next-generation smart footwear and wearable energy harvesting applications.

In addition to the electrical and mechanical optimizations proposed, future investigations will also consider long-term reliability aspects such as humidity resistance, sweat exposure, and mechanical fatigue. Predictive maintenance strategies, including in-field monitoring and anomaly detection algorithms [51], may be integrated in later stages to improve robustness and mitigate functional degradation in practical wearable applications.

Author Contributions: Conceptualization, M.L.M.A., G.A.G., M.d.M.A.C.M., A.A.G.S., O.H.A.J. and J.P.P.d.C.; methodology, M.L.M.A., G.A.G., and M.d.M.A.C.M.; software, M.L.M.A., and G.A.G.; validation, M.L.M.A., G.A.G., and M.d.M.A.C.M.; formal analysis, M.L.M.A., and G.A.G.; writing—original draft preparation, M.L.M.A., G.A.G., M.d.M.A.C.M., and A.A.G.S., O.H.A.J.; writing—review and editing, V.M., J.A.A., J.P.P.d.C. and J.L.A.; visualization, M.L.M.A., G.A.G., and M.d.M.A.C.M.; supervision, V.M., J.A.A., J.P.P.d.C. and J.L.A.; project administration, V.M., J.A.A., J.P.P.d.C. and J.L.A.; funding acquisition, V.M., J.A.A., J.P.P.d.C. and J.L.A. All authors have read and agreed to the published version of the manuscript.

Funding: This research was funded by CAPES grant number 88887.647931/2021-00, 88887.498688/2020-00, 88887.817116/2023-00 and Finance Code 001; National Council for Scientific and Technological Development (CNPq), grant numbers 402752/2023-6, 305858/2023-8, 402752/2023-6, 305858/2023-8 and 304113/2025-5; and by FAPESP under grants 2024/23815-4 and 2024/01120-4 (Assistive Technology Center for Daily Life Activities—CTECVIDA).

Data Availability Statement: Data are contained within the article.

Conflicts of Interest: The authors declare no conflicts of interest.

References

1. Katzir, S. The Discovery of the Piezoelectric Effect. *Arch. Hist. Exact Sci.* **2003**, *57*, 61–91. [CrossRef]
2. Lewis, T.J. The Piezoelectric Effect. In Proceedings of the 2005 Annual Report Conference on Electrical Insulation and Dielectric Phenomena, Nashville, TN, USA, 16–19 October 2005.
3. Cai, Y.; Song, S.; Xu, L.; Ma, J. Quasi-Monopole Ultrasound pulse transducer based on Piezoelectric ceramic material. In Proceedings of the 2021 IEEE 16th Nanotechnology Materials and Devices Conference, Vancouver, BC, Canada, 12–15 December 2021. [CrossRef]
4. Jiang, Z.; Dickinson, R.J.; Hall, T.L.; Choi, J.J. A PZT-PVDF Stacked Transducer for Short-Pulse Ultrasound Therapy and Monitoring. *IEEE Trans. Ultrason. Ferroelectr. Freq. Control* **2021**, *68*, 2164–2171. [CrossRef]
5. Zhang, Q.; Pang, X.; Zhang, Z.; Su, M.; Hong, J.; Zheng, H.; Qiu, W.; Lam, K.H. Miniature transducer using PNN-PZT-based ceramic for intravascular ultrasound. *IEEE Trans. Ultrason. Ferroelectr. Freq. Control* **2019**, *66*, 1102–1109. [CrossRef]
6. Madavarapu, J.B.; Islam, H.; Appathurai, A.; Safdar, G.A.; Muthukumaran, N.; Gnanamalar, J. Heterogeneous Energy Harvesting Techniques for Smart Home IoT Acceleration. *IEEE Access* **2024**, *12*, 73667–73675. [CrossRef]
7. Chandra, K.A.; Narayan, S.; Mamun, K.A.; Chand, A.A.; Prasad, D.; Ahmed, M.R. A Review of Footstep Energy Harvesting Systems. *IEEE Access* **2025**, *13*, 87149–87174. [CrossRef]
8. Li, X.; Li, Z.; Bi, C.; Liu, B.; Su, Y. Study on Wind Energy Harvesting Effect of a Vehicle-Mounted Piezo-Electromagnetic Hybrid Energy Harvester. *IEEE Access* **2020**, *8*, 167631–167646. [CrossRef]
9. Xiu, W.; Yao, Y.; Li, L.; Li, X.; Wu, J. A Novel Piezoelectric-Electromagnetic Vibration Energy Harvesting Device with Real-Time Adjustable Resonant Frequency. *IEEE Access* **2025**, *13*, 91215–91231. [CrossRef]
10. Yang, C.L.; Chen, K.W.; Chen, C.D. Model and Characterization of a Press-Button-Type Piezoelectric Energy Harvester. *IEEE/ASME Trans. Mechatronics* **2019**, *24*, 132–143. [CrossRef]
11. Khan, M.B.; Kim, D.H.; Han, J.H.; Saif, H.; Lee, H.; Lee, Y.; Kim, M.; Jang, E.; Joe, D.J.; Lee, K.J.; et al. A Harvesting Circuit for Flexible Thin-Film Piezoelectric Generator Achieving 562% Energy Extraction Improvement with Load Screening. *IEEE Trans. Ind. Electron.* **2021**, *68*, 12310–12321. [CrossRef]
12. Zhao, S.; Fu, H.; Ma, K.; Ma, J. A Novel Sensor for Vibration Frequency Measurement with Piezoelectric Kinetic Energy Harvesting. *IEEE Sens. J.* **2018**, *18*, 9286–9296. [CrossRef]
13. O'Donnell, J.; Sarkar, S.M.; Guerin, S.; Borda, G.G.; Silien, C.; Soulimane, T.; Thompson, D.; O'Reilly, E.; Tofail, S.A. Piezoelectricity in the Proteinogenic Amino Acid L-leucine: A Novel Piezoactive Bioelectret. *IEEE Trans. Dielectr. Electr. Insul.* **2020**, *27*, 1465–1468. [CrossRef]
14. Gong, C.; Xia, Z.; Han, R.; Qi, Z.; Feng, J.; He, Z.; Liu, H.; Gao, J.; Wei, Y.; Xu, Z. High-Efficiency Biomechanical Energy Harvesting Device with Enhanced Triboelectric Nanogenerator Performance Based on MXene Nanosheets Interfacial Polarization Strategy. *IEEE Sens. J.* **2025**, *25*, 2851–2860. [CrossRef]
15. Sessler, G.M. Bernhard Gross and the Evolution of Modern Electret Research. *Braz. J. Phys.* **1999**, *29*. [CrossRef]
16. Qiu, X.; Xia, Z.; Wang, F. Piezoelectricity of single-and multi-layer cellular polypropylene film electrets. *Front. Mater. Sci. China* **2007**, *1*, 72–75. [CrossRef]
17. Feng, Y.; Shao, B.; Tang, X.; Han, Y.; Wu, T.; Suzuki, Y. Improved Capacitance Model Involving Fringing Effects for Electret-Based Rotational Energy Harvesting Devices. *IEEE Trans. Electron Devices* **2018**, *65*, 1597–1603. [CrossRef]
18. Luo, A.; Zhang, Y.; Guo, X.; Lu, Y.; Lee, C.; Wang, F. Optimization of MEMS Vibration Energy Harvester With Perforated Electrode. *J. Microelectromech. Syst.* **2021**, *30*, 299–308. [CrossRef]
19. Li, M.; Luo, A.; Luo, W.; Wang, F. Recent Progress on Mechanical Optimization of MEMS Electret-Based Electrostatic Vibration Energy Harvesters. *J. Microelectromech. Syst.* **2022**, *31*, 726–740. [CrossRef]
20. Liu, Y.; Shi, Z.; Badel, A.; Miyoshi, T.; Suzuki, Y. Self-Powered Synchronous Electric Charge Extraction Rectifier for Rotational Electret Energy Harvester With Dual-Stage Electrodes. *IEEE Trans. Power Electron.* **2023**, *38*, 13166–13180. [CrossRef]
21. Ren, C.; Wang, K.; Zhang, P.; Li, Y.; Zhao, Z.; Shi, X.; Zhang, H.; Tao, K.; Yang, Z. A Self-Powered MEMS Inertial Switch for Potential Zero Power-Consumption Wake-Up Application. *J. Microelectromech. Syst.* **2021**, *30*, 550–559. [CrossRef]
22. Tao, K.; Lyu, B.; Zhang, J.; Li, Y.; Chang, H.; Yuan, W. Micro-Patterning of Electret Charge Distribution by Selective Liquid-Solid Contact Electrification. *J. Microelectromech. Syst.* **2022**, *31*, 625–633. [CrossRef]
23. Xi, X.; Zhao, Z.; Li, H.; Liao, C.; Chen, Y.; Pei, J.; Wang, L. Polarization-Induced Temperature Self-Sensing and Self-Powering Behavior of Carbon-Carbon Composites. *IEEE Sens. J.* **2024**, *24*, 20375–20385. [CrossRef]

24. Altafim, R.A.P.; Qiu, X.; Wirges, W.; Altafim, R.A.C.; Basso, H.C.; Gerhard, R.; Chinaglia, D.L.; Jenninger, W.; Wagner, J. Template-based fluoropolymer ferroelectrets with multiple layers of tubular channels. In Proceedings of the Annual Report—Conference on Electrical Insulation and Dielectric Phenomena, West Lafayette, IN, USA, 17–20 October 2010. [CrossRef]
25. Pisani Altafim, R.A.; Rychkov, D.; Wirges, W.; Gerhard, R.; Basso, H.C.; Corrêa Altafim, R.A.; Melzer, M. Laminated tubular-channel ferroelectret systems from low-density polyethylene films and from fluoroethylene-propylene copolymer films—A comparison. *IEEE Trans. Dielectr. Electr. Insul.* **2012**, *19*, 1116–1123. [CrossRef]
26. Palitó, T.T.C.; Assagra, Y.A.O.; Altafim, R.A.P.; Carmo, J.P.; Altafim, R.A.C. Hydrophone based on 3D printed polypropylene (PP) piezoelectret. *Electron. Lett.* **2019**, *55*, 203–204. [CrossRef]
27. De Luna, D.R.; Palitó, T.T.C.; Assagra, Y.A.O.; Altafim, R.A.P.; Carmo, J.P.; Altafim, R.A.C.; Carneiro, A.A.O.; De Sousa, V.A. Ferroelectret-based hydrophone employed in oil identification—A machine learning approach. *Sensors* **2020**, *20*, 2979. [CrossRef]
28. Pondrom, P.; Hillenbrand, J.; Sessler, G.M.; Bös, J.; Melz, T. Energy harvesting with single-layer and stacked piezoelectret films. *IEEE Trans. Dielectr. Electr. Insul.* **2015**, *22*, 1470–1476. [CrossRef]
29. Yang, H.; Pinto, R.M.R.; González-Losada, P.; Faraji, M.; Dias, R.; Vinayakumar, K.B. Geometry-optimized flexible ferroelectret fabricated by laser patterning of an adhesive spacer. *IEEE Sens. J.* **2024**, *24*, 9679–9686. [CrossRef]
30. Li, D.; Liu, W.; Zhu, B.; Qu, M.; Zhang, Q.; Fu, Y.; Xie, J. Machine learning-assisted multifunctional environmental sensing based on a piezoelectric cantilever. *ACS Sens.* **2022**, *7*, 2767–2777. [CrossRef] [PubMed]
31. Moreira, M.M.A.C.; Soares, I.N.; Assagra, Y.A.O.; Sousa, F.S.I.; Nordi, T.M.; Dourado, D.M.; Gounella, R.H.; Carmo, J.P.; Altafim, R.A.C.; Altafim, R.A.P. Piezoelectrets: A brief introduction. *IEEE Sens. J.* **2021**, *21*, 22317–22325. [CrossRef]
32. Hillenbrand, J.; Sessler, G.M. Stacked piezoelectret microphones of simple design and high sensitivity. *IEEE Trans. Dielectr. Electr. Insul.* **2006**, *13*, 973–979. [CrossRef]
33. Zhang, M.; Xiang, X.; Zhang, X.; Dai, Y. Tape-like vibrational energy harvesters using flexible fluorinated polyethylene propylene (FEP) piezoelectret as transduction material. *IEEE Trans. Dielectr. Electr. Insul.* **2022**, *29*, 768–775. [CrossRef]
34. Wang, Y.; Wu, L.; Zhang, X. Energy harvesting from vibration using flexible fluoroethylenepropylene piezoelectret films with cross-tunnel structure. *IEEE Trans. Dielectr. Electr. Insul.* **2015**, *22*, 1349–1355. [CrossRef]
35. Yang, R.; Ma, Y.; Cui, J.; Liu, M.; Wu, Y.; Zheng, H. Nano PDA@Tur-modified piezoelectric sensors for enhanced sensitivity and energy harvesting. *ACS Sens.* **2024**, *9*, 3137–3149. [CrossRef] [PubMed]
36. Xue, Y.; Li, S.; Zhang, M.; Ruan, Z.; Wu, K.; Cao, J.; Li, G.; Zhang, X.; Fang, P. Air-borne ultrasonic transducers based on cross-linked polypropylene ferro/piezoelectrets. *IEEE Sens. J.* **2022**, *22*, 14806–14814. [CrossRef]
37. Martins, A.; Pinheiro, M. On the propulsive force developed by asymmetric capacitors in a vacuum. *Phys. Procedia* **2011**, *20*, 112–119. [CrossRef]
38. Laganà, F.; Faccì, A.R. Parametric optimisation of a pulmonary ventilator using the Taguchi method. *J. Electr. Eng.* **2025**, *76*, 265–274. [CrossRef]
39. Qian, Z.; Ren, L.; Ding, Y.; Hutchinson, J.R.; Ren, L. A Dynamic Finite Element Analysis of Human Foot Complex in the Sagittal Plane during Level Walking. *PLoS ONE* **2013**, *8*, e79424. [CrossRef]
40. Costa, M.; Peng, C.K.; Goldberger, A.L.; Hausdorff, J.M. Multiscale entropy analysis of human gait dynamics. *Phys. A Stat. Mech. Its Appl.* **2003**, *330*, 53–60. [CrossRef]
41. Keller, T.; Weisberger, A.; Ray, J.; Hasan, S.; Shiavi, R.; Spengler, D. Relationship between vertical ground reaction force and speed during walking, slow jogging, and running. *Clin. Biomech.* **1996**, *11*, 253–259. .. [CrossRef]
42. Ando Junior, O.H.; Maran, A.L.O.; Henao, N.C. A review of the development and applications of thermoelectric microgenerators for energy harvesting. *Renew. Sustain. Energy Rev.* **2018**, *91*, 376–393. [CrossRef]
43. Ando Junior, O.H.; Sylvestrin, G.R.; Scherer, H.F. Experimental Validation of State of Charge Estimation by Extended Kalman Filter and Modified Coulomb Counting. *IEEE Lat. Am. Trans.* **2022**, *20*, 2395–2403. [CrossRef]
44. Sylvestrin, G.R.; Scherer, H.F.; Ando Junior, O.H. Hardware and Software Development of an Open Source Battery Management System. *IEEE Lat. Am. Trans.* **2021**, *19*, 1153–1163. [CrossRef]
45. Silva, E.A.d.; Urzagasti, C.A.; Maciel, J.N.; Ledesma, J.J.G.; Cavallari, M.R.; Ando Junior, O.H. Development of a Self-Calibrated Embedded System for Energy Management in Low Voltage. *Energies* **2022**, *15*, 8707. [CrossRef]
46. Crecraft, D.I.; Gergely, S. 2—Signals and signal processing. In *Analog Electronics*; Elsevier: Amsterdam, The Netherlands, 2002; pp. 13–71. [CrossRef]
47. DuPont. *DuPont™ Teflon® FEP Fluoroplastic Film Properties Bulletin*; Properties bulletin; DuPont: Wilmington, DE, USA, 2013.
48. de Assis, S.C.; Morgado, D.L.; Scheidt, D.T.; de Souza, S.S.; Cavallari, M.R.; Ando Junior, O.H.; Carrilho, E. Review of Bacterial Nanocellulose-Based Electrochemical Biosensors: Functionalization, Challenges, and Future Perspectives. *Biosensors* **2023**, *13*, 142. [CrossRef] [PubMed]
49. Ando Junior, O.H.; Silva, E.A.d.; Lira, E.R.d.; Degiorgi, S.V.B.; Carmo, J.P.P.d. Comparative Analysis and Integrated Methodology for the Electrical Design and Performance Evaluation of Thermoelectric Generators (TEGs) in Energy Harvesting Applications. *Energies* **2024**, *17*, 5176. [CrossRef]

50. Ando, O.H.; Izidoro, C.L.; Gomes, J.M.; Correia, J.H.; Carmo, J.P.; Schaeffer, L. Acquisition and Monitoring System for TEG Characterization. *Int. J. Distrib. Sens. Netw.* **2015**, *11*, 531516. [CrossRef]
51. Prattico, D.; Laganá, F.; Oliva, G.; Fiorillo, A.S.; Pullano, S.A.; Calcagno, S.; De Carlo, D.; Foresta, F.L. Sensors and Integrated Electronic Circuits for Monitoring Machinery on Wastewater Treatment: Artificial Intelligence Approach. In Proceedings of the 2024 IEEE Sensors Applications Symposium (SAS), Naples, Italy, 23–25 July 2024; pp. 1–6. [CrossRef]